

Research Paper

3D multiphysics modeling for probing the non-homogenous parameter distribution in proton exchange membrane electrolyzer cells



Weitian Wang^a, Jun Li^a, Lei Ding^a, Jiajie Wu^b, Hang Ma^b, Tony Shi^b, Matthew Mench^a, Feng-Yuan Zhang^{a,*}

^a Department of Mechanical, Aerospace & Biomedical Engineering, University of Tennessee, Knoxville, Knoxville, TN 37996, USA

^b Department of Industrial and Systems Engineering, University of Tennessee, Knoxville, Knoxville, TN 37996, USA

ARTICLE INFO

Keywords:
PEM electrolyzer
Multiphysical modeling
Porous transport layers
Current distribution
Local dehydration

ABSTRACT

Mass transport processes play a significant role in the proton exchange membrane electrolyzer cells (PEMECs) to produce affordable “green hydrogen”. However, the strong interaction among components of PEMECs results in complex transport processes, involving multiple mass, phase, and scale, which is challenging to be experimentally probed. Herein, we developed a fully validated 3D multiphysics model to describe and predict the correlation between component designs and critical parameters of PEMECs. It is found that the water saturation and current density are not evenly distributed, which significantly depends on the interaction among anode bipolar plates (BPs), porous transport layers (PTLs), and thickness of PEMs. On one hand, the wide lands of anode BPs will partially block the pores of PTLs and cause a severe local dehydration and current density drop, which can be addressed by decreasing the width of BP lands or a flow enhanced liquid/gas diffusion layer (FELGDL) design. On the other hand, a thinner PEM tends to cause a worse uniformity of water and current density distribution in PEMs, though better cell performance is promised. Overall, the presented model provides much localized insights and their impacts on the overall performance of PEMECs, which helps the component design and integration of PEMECs in the future.

1. Introduction

Large-scale production of affordable “green hydrogen” has been regarded as one of the most promising strategies to realize a carbon neutral society in the future [1]. To realize this mission, the development of high-efficiency and low-cost “green hydrogen” generators, such as the proton exchange membrane electrolyzer cells (PEMECs), is the primary challenge to be addressed [2]. Recently, various strategies aiming at efficiency improvement and cost reduction of PEMECs are proposed. Among these strategies, the redesign of critical porous transport layers (PTLs) is undoubtedly at the center of the stage. The commercial PTLs mainly include Ti felt and sintered Ti powders [3]. These PTLs act as the transport media for water, gas, electron, and heat, which guarantee high-efficiency electrochemical reactions [4,5]. However, the limitation of the conventional PTLs hinder further improvement of hydrogen production efficiency and costs, that is, the complex and narrow pore networks inside conventional PTLs result in a relatively large transport resistance for water and gas [4,6]. As a result, local

dehydration is very likely especially at high current densities. For example, Zlobinski *et al.*, *in-situ* measured the water saturation across the cross section of a commercial sintered Ti powders PTL using a neutron beam. They found that the water saturation in the PTL/CCM interface is as low as ~50 % even at a very small current density [7]. Addressing the local transport challenge is highly desired for the “green hydrogen” production community. Recently, advanced 2D structured PTLs attracted much attention due to their high-performing mass transport properties and electrochemical properties in PEMECs. Kang *et al.*, for the first time, reported the novel thin/tunable liquid/gas diffusion layer (TTLGDL) with large and through pores [6]. The electrochemical performance of TTLGDLs outperformed most of the previous publications. Inspired by the discovery of real electrochemical reaction sites by Mo *et al.*, directly coating catalysts on the 2D structured PTLs realized a dramatic catalyst saving and efficiency enhancement simultaneously [8]. Following studies found that the open and straight through pores of 2D PTLs greatly boost the gas release compared with the conventional PTLs [4].

* Corresponding author.

E-mail address: fzhang@utk.edu (F.-Y. Zhang).

Although, the advantages of 2D PTLs have been validated by various publications, the absence of in-plane transport pathways for 2D PTLs still raises a concern of gas blockage under the bipolar plates (BPs). Wang *et al.*, designed a unique interface-visible characterization cell (IV-CC) for the observation of gas accumulation in the electrode/membrane interface. It is directly observed that the BP blockage will cause a rapid and complete gas blockage in the pores of 2D PTLs as shown in Fig. 1a. Even for the 3D-structured Ti felt PTL, the local gas blockage is still very likely in the electrode/membrane interface [9]. The observed local gas blockage is not the result of a single component design, but the results of interaction among the BP, PTL, and PEM in PEMECs, which is unexpected and less understood. Understanding the correlation between component design (PTLs, PEMs, BPs, etc) and electrochemical performance of PEMECs is critical for the design of advanced PTLs and the optimization of cell configurations in the future.

Numerical modeling is an useful tool for assessing the performance of different designs and gaining insights through simulation that cannot be directly probed in physical experiments, such as the micro-scale water transport inside the PTL [10]. Some efforts have been made for modeling PEMECs in various scopes and focus. Han *et al.*, established a 0D two-phase transport model for simulating the impacts of current density, contact angle, porosity, and thickness, on the liquid water transport/saturation, voltage and efficiency in a PEMEC [11]. Kang *et al.*, developed a 2D model to investigate the nonhomogeneous current distribution caused by the low conductivity of the catalyst layer. Wrubel *et al.*, also proposed a 2D multiphysics model to enhance the understanding how the pore alignment will impact the performance of PEMECs [10]. Most of the developed models are 0D or 2D, however, the realistic PEMECs are always 3D, which is hardly to be fully described by a 0D or 2D model. Hence, a multiphysics model for describing the component interaction in the 3D level is highly desired for the water electrolyzer community.

This study proposes a 3D numerical model for PEMECs to describe and predict the correlation between component designs and critical parameters of PEMECs. The proposed model is validated with polarization curves and high frequency resistance (HFR) curves simultaneously. The validated model is utilized to investigate the interaction among

components and their correlation with the electrochemical performance of PEMECs. With the help of the fully validated model, the uneven water and current density distribution in PEMECs are unveiled at various operation conditions. These insights highlight the non-homogeneous phenomena caused by the local geometry, which need to be carefully considered for the development of advanced transport medias in PEMECs.

2. Numerical method

The whole PEMECs are described by highly coupled electrochemical reaction equations, mass transport equations, and electrical equations. To simplify the numerical model, some reasonable assumptions are made based on references or experimental observation. Firstly, the catalyst layers are simplified to a 2D case instead of 3D, that is, the thickness of Ir film is neglected in this model. This assumption is made since the electroplated Ir film only has a thickness of <100 nm, which is much smaller than the typical thickness (~10 μm) of conventional ionomer-mixed catalyst layers and the size of mesh [12,13]. Hence, this assumption is expected to be reasonable. Secondly, in the open pore area of anode electrode, it is assumed that the PEM well contact with the bulk water in the flow channels. This assumption is based on experimental observation. Due to the unique thin and through pores of the TTLGDL, the very low aspect ratio causes a very easy water touch on the PEM in open pore areas of the TTLGDL, which could be validated by videos in previous publications [4,14]. Finally, the channels of cathode BP is assumed to be filled with vapor saturated hydrogen. Although no water flow was introduced to the cathode BP, cathode side is still a water-rich environment due to the continuous electroosmotic flow from anode to cathode [15,16]. It has been observed that the water saturation in the cathode PEM interface even is higher than the anode interface of PEMs [7].

2.1. Electrochemical governing equations

The overall potential of PEMECs is described by thermodynamic potential, activation overpotential, and ohmic overpotential as shown in

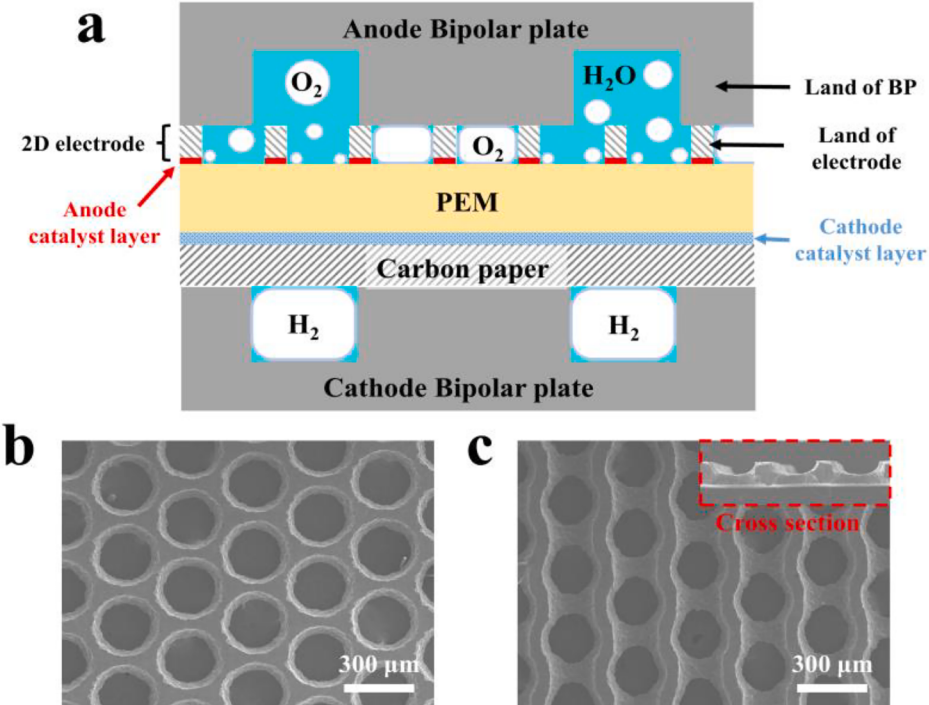


Fig. 1. a) Schematic of the simulated PEMEC assemblies; b) SEM image of 2D-structured TTLGDL; c) SEM images of 3D-structured FELGDL with cross section.

Eq. (1) [17,18].

$$V_{cell} = V_{th} + \eta_{act} + \eta_{ohm} \quad (1)$$

Where V_{cell} is the overall potential of PEMECs, V_{th} is the thermodynamic potential, η_{act} is the activation overpotential, η_{ohm} is the ohmic overpotential. The physical meaning and calculation for each potential will be described in the following content. The thermodynamic potential is determined using the Nernst equation [16]:

$$V_{th} = V_0 + \frac{RT}{n_a F} \ln\left(\frac{\alpha_{H2}\alpha_{O2}^{0.5}}{\alpha_{H2O}}\right) \quad (2)$$

$$V_0 = 1.5184 - 1.5421 \times 10^{-3}T + 9.523 \times 10^{-5}T \ln(T) + 9.84 \times 10^{-8}T^2 \quad (3)$$

where R is the gas constant (8.314 J/ (mol K)), T is the temperature (353.15 K), n_a is the transferred electrons per 1 product molecule, which is 4 for OER; α_{H2} is the activity of hydrogen, α_{O2} is the activity of oxygen, α_{H2O} is the activity of water. F is the Faraday's constant (96,485 C/mol); V_0 is the standard thermodynamic potential at the standard temperature and pressure. The later item is a correction for systems under non-standard conditions. Notably, concentration impacts the overall cell voltage in the aspects of both thermodynamics and kinetics. Some publications separate the later item of Eq. (2) as a diffusion loss, which is equivalent to the formulas in this study. The concentration impacts on the reaction kinetics will be described in equations (4) and (5).

The OER and HER current density are calculated by the Butler-Volmer (B-V) equation [19]. The Anode OER current density (A/cm^2) j_a and Cathode current density j_c are given below:

$$j_a = j_{0,a} (a_{R,a} \exp\left(n_a \frac{\alpha_a F}{RT} \eta_{act,a}\right) - a_{P,a} \exp\left(-n_a \frac{(1-\alpha_a)F}{RT} \eta_{act,a}\right)) \quad (4)$$

$$j_c = j_{0,c} (a_{R,c} \exp\left(n_c \frac{\alpha_c F}{RT} \eta_{act,c}\right) - a_{P,c} \exp\left(-n_c \frac{(1-\alpha_c)F}{RT} \eta_{act,c}\right)) \quad (5)$$

$j_{0,a}$ is the exchange current density of OER; $a_{R,a}$ and $a_{P,a}$ are the activity of reactant and production of OER, respectively; α_a is the charge transfer coefficient of OER; $\eta_{act,a}$ is the overpotential of OER. For the HER side, the meaning of these parameters is the same, but are named by "c", instead of "a". For OERs/HERs, the kinetic parameters of B-V equation are highly controversial due to different catalyst materials and measurement conditions [16]. For example, the reported anode exchange current densities range from 10^{-1} to $10^{-13} A/cm^2$ [16]. Hence, researchers usually pick the kinetic parameters for the best fitting. Considering the similar material, the OER exchange current density and charge transfer coefficient with metallic Ir reported by Lu *et. al.* are selected [20]. Kinetic parameters are shown in Table 1.

2.2. Transport of electrons, protons, water, and gas

In this study, the transport of electrons, protons, water, and gas is considered. Both electron and proton transport follow the Ohm's law as shown in equation (6).

$$j_i = \sigma_i \nabla \Phi_i \quad (6)$$

Where j_i is the electron/proton current density (A/m^2), σ_i is the local

conductivity of the electron/proton, Φ_i is the potential. The electron-conductive phase includes anode/cathode BP, anode PTL, and cathode GDL. For the PEM, the proton conductivity heavily depends on the water saturation. The correlation between proton conductivity of PEMs and water saturation is described by equation (7)[10].

$$\sigma_{PEM} = \lambda + 2.5 \quad (7)$$

σ_{PEM} is the conductivity of membranes (S/m). The water saturation (λ) is a dimensionless parameter defined by the ratio of water concentration (c_w) and the concentration of sulfuric acid group (c_f)[21].

$$\lambda = \frac{c_w}{c_f} \quad (8)$$

Appling the mass conservation law on equation (6), in the bulk conductive phase, the divergence of j_i is 0 as shown in equation (9). In the anode reaction interface, both electron and proton conductive phase have source terms ($-\dot{R}_a$), while the sink terms are applied in the cathode side (\dot{R}_c) as shown in Eqs. (10) and (11), respectively.

$$\nabla \cdot j_{i,bulk} = 0 \quad (9)$$

$$\nabla \cdot j_{i,anode} = -\dot{R}_a \quad (10)$$

$$\nabla \cdot j_{i,cathode} = \dot{R}_c \quad (11)$$

The water transport in PEMs is mainly governed by diffusion flow, electroosmotic flow, and permeation flow. The permeation flow is driven by the pressure difference between anode and cathode of PEMECs. In this study, the pressure is in equilibrium. Hence, the permeation flow is not considered. The diffusion flow is driven by the concentration gradient of water, which is governed by Fick's law.

$$J_{w,D} = D_w \nabla c_w \quad (12)$$

where $J_{w,D}$ ($mol s/m^2$) is the molar flux of water, D_w (m^2/s) is the diffusion coefficient of water in PEMs, c_w (mol/m^3) is the concentration of water in PEMs. D_w is a function of c_w , and can be described by equation (13)[22].

$$D_w = 3.10 \times 10^{-7} \times \lambda \times (\exp(0.28\lambda) - 1) \times \exp\left(-\frac{2436}{T}\right), 0 < \lambda < 3 \quad (13)$$

$$D_w = 4.17 \times 10^{-8} \times \lambda \times (161 \times \exp(-\lambda) + 1) \times \exp\left(-\frac{2436}{T}\right), \lambda \geq 3 \quad (14)$$

The electroosmotic flow is the result of proton transport, which is proportional to the number of protons.

$$J_{w,EO} = n_d j_p \quad (15)$$

where $J_{w,EO}$ ($mol s/m^2$) is the mola flux of water, n_d is the electroosmotic coefficient of water in PEMs, j_p (A/m^2) is the current density of protons. n_d is closely related to the local water saturation of PEMs, which can be described by the following empirical formula [23]:

$$n_d = \frac{2.5}{\lambda_{le}} \lambda \quad (16)$$

In the bulk PEM domain, mass conservation is applied on water transport.

$$\nabla \cdot (D_w \nabla c_w + n_d j_p) = 0 \quad (17)$$

In the anode and cathode boundary, water source or sink may apply.

$$\nabla \cdot (D_w \nabla c_w + n_d j_p) = \dot{R}_w \quad (18)$$

Table 1
Kinetic parameters of B-V equation.

Parameters	Description	Value
$j_{0,a}$	Anode exchange current density	$1.99 \times 10^{-11} A/cm^2$ [20]
α_a	Anode charge transfer coefficient	0.61 [20]
$j_{0,c}$	Cathode exchange current density	$0.02 A/cm^2$ [16]
α_c	Cathode charge transfer coefficient	0.5 [16]

For a liquid-equilibrated PEM boundary, the interfacial water transport resistance can be neglected, which means that the water saturation of PEM is always 100 % for this case [24–26]. For a vapor-equilibrated PEM boundary, the source term of \dot{R}_w is calculated by the equations presented by Ge et al [27].

$$\dot{R}_w = k_{w,a} c_f (\lambda_{ve} - \lambda) \quad (19)$$

where $k_{w,a}$ is the mass transfer coefficient (m/s) for water absorption, and λ_{ve} refers to the vapor-equilibrated water saturation of PEMs.

2.3. Boundary conditions

The potential of the very top surface of anode and cathode BP is set as overall cell voltage and 0 V, respectively. The pressure in anode and cathode flow channels is atmospheric pressure. The proton/electron conductivity of electron/proton-conductive phase is assumed to be zero. For the PEM, the water concentration in the anode open pores is Dirichlet conditions and the water concentration in cathode and blocked anode pores are Neumann conditions.

2.4. Software and solver

All the equations are implemented in a commercially available COMSOL Multiphysics 6.1 using a mathematic module. The PARDISO solver was employed to solve the static model with a separation technique. The iteration was stopped until the residual is less than 0.001. The mesh independent test was conducted by adjusting the mesh density. The mesh independent test results are shown in Figure S1. The final mesh scale is around 1.5 million elements. The structure of the mesh is shown in Figure S2.

3. Experimental setup

3.1. Cell assembly for experimental tests

The performance of two anode electrodes is experimentally evaluated in the same standard PEMECs. The Ir catalysts are electrodeposited on TTLGDL and FELGDL substrates following the protocol as described by our previous publications [12,14]. The manufacturing process for the TTLGDL and FELGDL can be found in previous publications [3,28]. The catalyst coated TTLGDL and FELGDL electrodes share the same final Ir loading of ~ 0.28 mg/cm², working as the anode electrodes. Commercial proton exchange membranes coated with hydrogen evolution reaction (HER) catalyst layers from Nel Hydrogen (Wallingford, CT) were employed as the electrolyte and cathode electrode. Carbon papers with a thickness of 280 μm were applied as the cathode gas diffusion layer (GDL). The whole membrane electrode assembly was sandwiched by the anode and cathode bipolar plates (BPs). The cathode BP is made from graphite, and the anode BP is made from grade 2 Ti due to the high-oxidizing anode environment. The clamping pressure is provided by two stainless steel end plates, fastening by eight evenly distributed bolts (4.5 N m torque on each bolt). All the PEMECs were tested under the temperature of 80 °C. Polarization curves and high frequency resistance (HFR) curves are collected by a potentiostat (VSP/VMP-100, BioLogic).

3.2. Study cases

For the experimental section, two different anode electrodes are tested in the same conditions. These two anode electrodes have the same catalyst layer but different PTL substrates. One of the electrodes has a 2D-structured TTLGDL as the PTL substrate (Fig. 1b), while another one has a 3D-structured FELGDL with parallel in-plane channels as substrate (Fig. 1c). Two corresponding numerical study cases are developed to describe the experimental data of TTLGDL and FELGDL cases. To avoid confusion, the solid parts of anode BP and electrodes are described as

“the land of BP” and “the land of electrode”, respectively, as shown in Fig. 1.

4. Results and discussion

4.1. Model validation with polarization curves and high frequency resistance curves

To validate the the feasibility of the developed numerical model, both polarization curves and high frequency resistance (HFR) curves are experimentally collected as shown in Fig. 2a and b. Overall, the FELGDL electrode shows an improved polarization curve compared with the TTLGDL cell, attributing to the improved water/gas transport under the BP lands. Interestingly, the HFR curve of TTLGDL case shows an obvious increase trend along the current density, while the FELGDL can significantly suppress this increase trend. It is assumed that the improved water/gas transport under BP lands helps improve the water saturation of the PEM under BP land. This HFR curve trend is successfully captured by our model, and the underlying mechanism will be discussed in the following sections.

In most publications related with the modeling of water electrolyzers, polarization curve validation is widely employed. However, the significance of HFR validation is overlooked for a long time. In PEMECs, HFR curves reflect the total ohmic resistance, consisting of proton transport resistance in ionomer phase, electron transport resistance in electron conductors, and the interface resistances. The correct interpretation of HFR provides more insights about the parameter changes in PEMECs, especially when the water dehydration is taken into consideration. The numerical model presented in this manuscript are fully validated by both polarization curves and HFR curves, which makes the analysis and prediction results convincing. It could be concluded that both simulated polarization and HFR curves match well with the experimental collected curves, even after switching the electrode design from TTLGDL case to FELGDL case. For the TTLGDL case, a limited deviation between experimental and simulated data is observed as shown in Fig. 2b. The simulated data overestimated the HFR. The reason might be TTLGDL pores under BP lands were not completely blocked due to the surface roughness of TTLGDL and BP lands. The roughness of the contact interface may provide limited water transport pathways and finally improve the hydration of the membrane, which might be the source of error.

4.2. Water profile in PEMs

Given the water-rich environment in PEMECs, most publications simplify the calculation of water saturation in PEMs by assuming 0D or 1D cases. In other words, the entire PEM is assumed to be fully hydrated (0D), or water hydration is considered to change only along the through-plane direction (1D). However, various recent studies implied that the feasibility of this assumption might not be universal in PEMECs, especially for the high-current density operation, which is difficult to measure by experimental techniques [9]. Our numerical models can provide critical insights into the water profile in PEMs as shown in Fig. 3.

Four cross-sections in different normalized z positions are selected to probe the water profiles as shown in Fig. 3a. The numerical calculation domain includes six rows of 2D pores. The middle two rows are located under the lands of anode BP, and the others are under the channel area. It could be found that the land of anode BP causes a significant dehydration inside PEMs, while the impact of BP lands gradually alleviates from anode to cathode side. Two typical x-cross sections at the land and channel of BP are plotted in Fig. 3b and c, respectively. It is found that the pattern of anode electrode causes a non-homogeneous water distribution in the PEM, except for the impacts of BP lands. On one hand, the reaction interface between anode electrode and the PEM continuously consumes water. In the pore edge of electrode, the consumed water can be supplied by the bulk liquid water inside PTL. However, the bulk

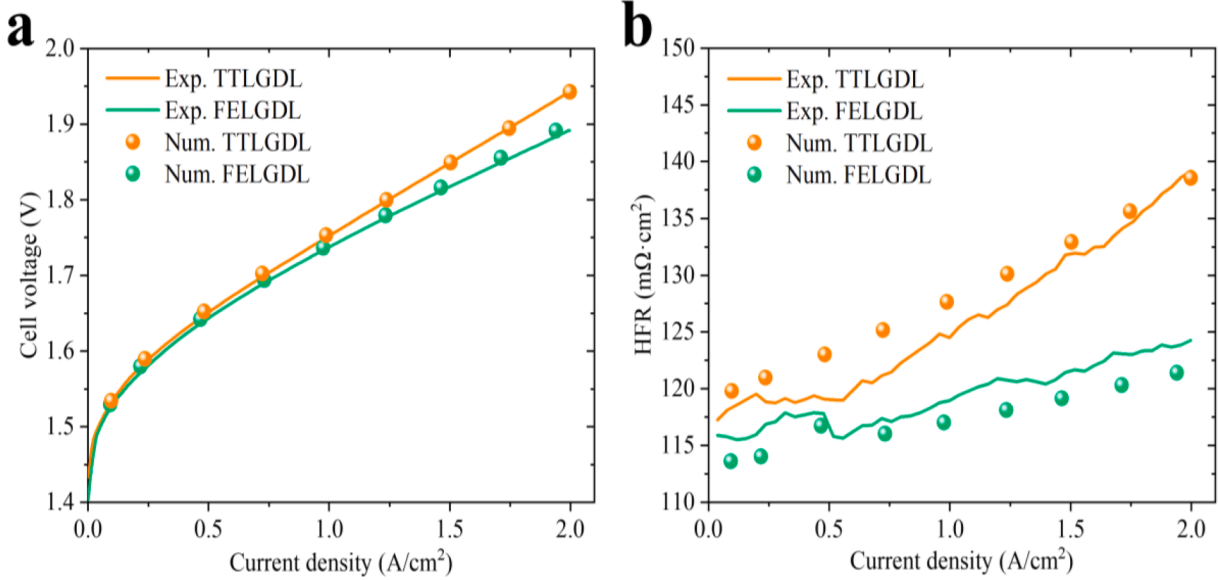


Fig. 2. Model validation of experimental data. (a) polarization curve validation, and (b) high-frequency resistance (HFR) validation.

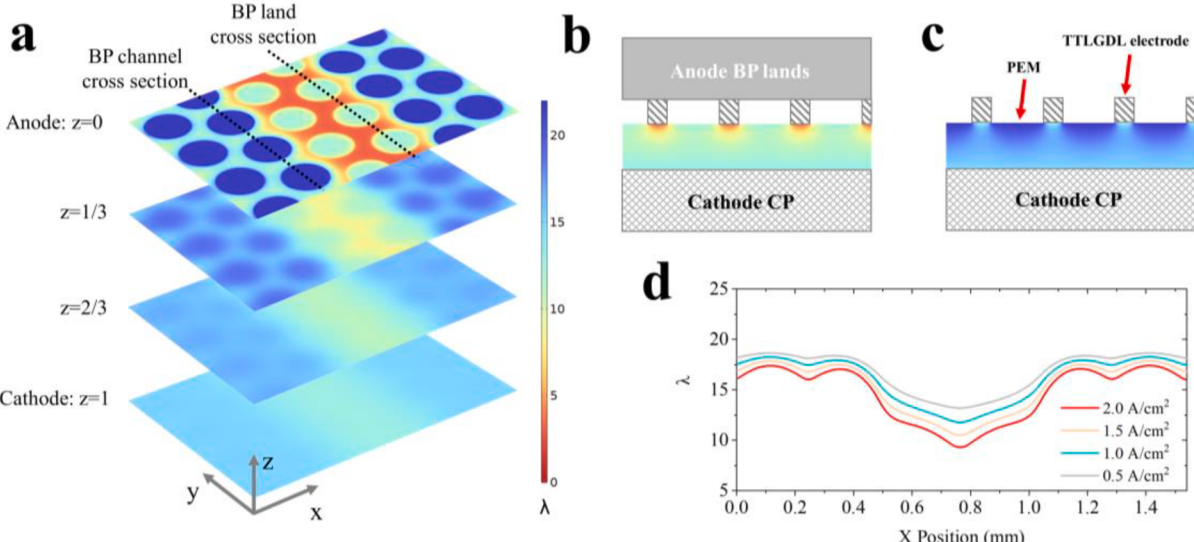


Fig. 3. Water distribution inside the PEM. a) water profile of selected z-cross section; b) water profile in selected x-cross section under BP land (“BP land cross section” in Fig. 3a); c) water profile in selected x-cross section under BP channel (“BP channel cross section” in Fig. 3a); d) average water saturation in x direction at different overall current densities. (All figures share the same color bar).

liquid water supply to inner area of electrode/PEM interface will be limited due to the limits of water transport pathways. For the given electrode pattern in this study, water must travel up to $\sim 20 \mu\text{m}$ to reach the inner reaction interface. Hence, the water in the PEM is expected to act as an important water source for the oxygen generation reaction (OER)[9]. On the other hand, travel of protons will be accompanied by water molecules, which is well known as the electro-osmosis flow. These two sinks together result in water dehydration in the reaction interface. In the BP land area, the insufficient water supply from the pores of PTLs intensifies the water dehydration in the reaction interface (Fig. 3b) compared with the BP channel area (Fig. 3c).

Fig. 3d gives the quantified average water distribution along the x direction at different current densities. Impacts of both electrode pattern and BP land can be observed. It can be found that the BP lands cause a significant drop in water saturation. At the current density of $2 \text{ A}/\text{cm}^2$, the average water saturation is only ~ 12 under the land area, while the

average level in the channel area is ~ 17 . Compared with the BP lands, the land of electrode only causes a slight drop in water saturation. At lower current densities, the water hydration level will be higher and more uniform.

4.3. Current density distribution in PEMs

Ohmic resistance of PEMs closely relates to the hydration level. A higher water saturation helps the conduction of proton inside PEMs, as described by the vehicle mechanism or hopping mechanism [21]. Thus, it can be expected that the non-uniform water saturation directly results in different local ohmic resistance, then leads to a non-homogenous current density distribution inside the PEM as shown in Fig. 4. To investigate the impacts of BP lands and electrode lands, typical middle cross sections ($z = 0.5$) are extracted at different overall current densities as shown in Fig. 4a. It is found that the uniformity of current

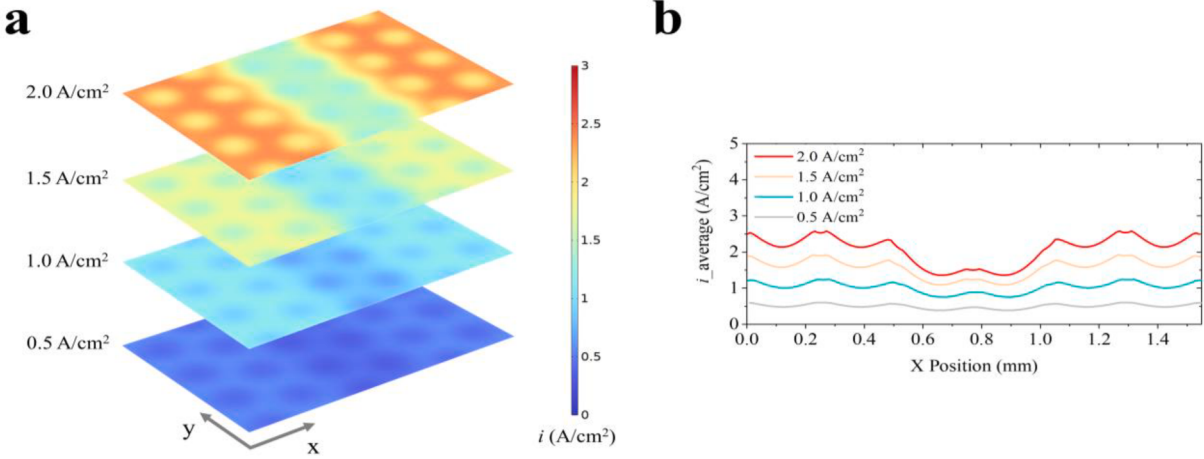


Fig. 4. A) current density distribution inside the pem; d) average current density in x direction at different overall current densities.

densities decreases along the increase of overall current densities. This phenomenon is mainly caused by both BP lands and electrode lands, which is consistent with the water distribution in the PEM. Notably, the pattern of anode electrode significantly impacts the current density distribution inside the PEM. The pore area has an obvious lower current density, while the current density under the land of electrode is much larger. Fig. 4b shows the average current density inside the PEM along x direction for different overall current density cases. At a relatively low overall current density of $0.5 \text{ A}/\text{cm}^2$, the BP land has limited impact on the current density distribution. When the overall current density increases to $2 \text{ A}/\text{cm}^2$, a severe local current density drop is observed under the land of BP. Increasing the overall current density from 0.5 to 1.0, 1.5, and $2.0 \text{ A}/\text{cm}^2$, the standard deviation (STD) of local current densities increases from 0.06 to 0.14, 0.26, and $0.39 \text{ A}/\text{cm}^2$. It could be concluded that a higher current density will result in the increase of non-uniformity of local current density due to the feature of BP lands and electrode lands. Under the land area of BPs, the lower local current density is mainly caused by the high local ohmic resistance of the PEM due to local dehydration.

4.4. Local pore blockages

For 2D-structured PTLs, the absence of in-plane transport will cause local pore blockage, which is a well-recognized concern in the PEMEC community, as discussed earlier. The reason is some PTL pores are blocked by the lands of BPs, and the water supply from BP channel is not accessible for blocked pores. However, the locally blocked pores don't mean complete stop of reaction due to the existence of water supply pathways inside the PEM [9]. The correlation between the pore blockage and cell performance is not well understood yet.

Ideally, all the pores of PTL should be open to the flow channels of BP, which is the case of FELGDL as shown in Fig. 5. Taking two experimental cases (TTLGDL and FELGDL) as examples, the benefits of open pores are revealed at the same applied cell voltage of 1.94 V. As shown in Fig. 5a and b, the FELGDL design can significantly improve the local current density and water saturation drop under the lands area of anode BPs. It could be found that the local pore blockage of TTLGDL can significantly degrade the local current density from $\sim 2.3 \text{ A}/\text{cm}^2$ to $\sim 1.5 \text{ A}/\text{cm}^2$ at the same cell voltage as shown in Fig. 5c. In the channel area of

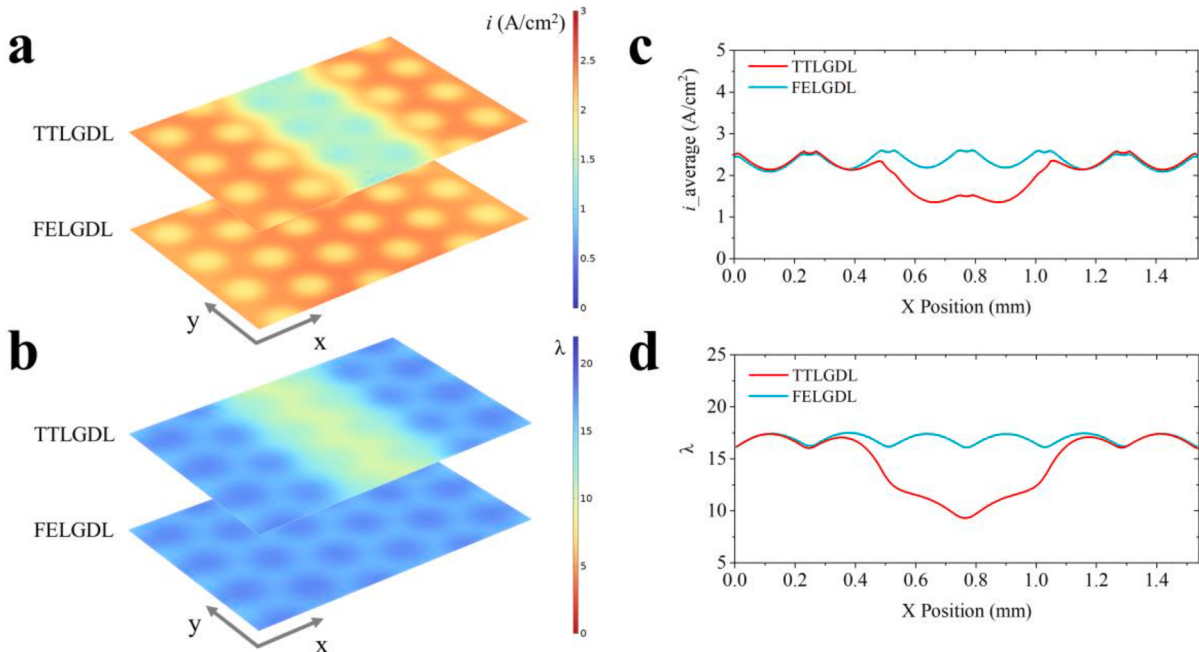


Fig. 5. A) current densities profile and b) water saturation profile of ttlgdl and felgdl; c) average current density and d) average water saturation in x direction at an applied cell voltage of 1.94 V.

BP, the TTLGDL and FELGDL share a very similar local current density due to the similar electrode pattern and mass transport. For water saturation, the pore blockage of TTLGDL results in local water starvation, from ~ 17 to ~ 12 as shown in Fig. 5d. It can be concluded that the performance improvement of FELGDL design originates from the improved mass transport for the blocked pores in TTLGDL, which theoretically explained the experimental data in Fig. 2.

To quantify the impact of local pore blockage on the overall cell performance, cases with different ratio of open pores are simulated as shown in Fig. 6 at the same cell current density of 2 A/cm^2 . The ratio of open pores (ROP) is defined as the ratio between pores without BP land blockage and total pores in PTLs. A larger ROP indicates more pores are open to the flow channel, while a smaller ROP means more pores are blocked by the lands of BPs. For the FELGDL case the ROP is assumed to be 1, which means all the pores of FELGDL are open due to their in-plane channels. For the TTLGDL case, the ROP is $1/3$. It could be found that the cell voltage significantly increases with the decrease of the ROP (pores without BP land blockage). For example, decreasing the ROP from 1.0 to 0.2 the cell voltage will increase $\sim 200 \text{ mV}$ at 2 A/cm^2 , which is a severe performance loss for PEMECs. Previous publications demonstrated the decreased local current density under the BP land area compared with BP channel area. For example, Chen et al. observed a severe local current decrease under the lands of BP compared with channel area [29]. In this study, we evaluate the impacts of local pore blockage on the whole-cell performance for the first time. Addressing the local gas blockage in the electrode/PEM interface is critical to promise good cell performance. Notably, the operation conditions of PEMECs are various. The model needs to be adjusted accordingly to precisely predict the pore blockage impacts for PEMECs with different cell assembly or operation parameters.

4.5. Thickness of PEMs

The PEM is a core transport media for protons in PEMECs. Commercially available PEMs have typical thicknesses of $50 \mu\text{m}$, $127 \mu\text{m}$, and $183 \mu\text{m}$. A thinner PEM has the advantage of smaller ohmic resistance, but a larger hydrogen crossover rate from cathode to anode, which raises the concern of safety. The thicker PEM is safer but the relatively large ohmic resistance will decrease the hydrogen production efficiency. However, as a solid electrolyte, it is found that the current distribution in the PEM could be affected by the PEM thickness as shown in Fig. 7a. The current distribution in a thicker PEM is more uniform compared with the thinner one as shown in Fig. 7b. For the $50\text{-}\mu\text{m}$ PEM case, both BP lands and pattern of anode electrodes have significant

impacts on the current distribution. In the area corresponding to pore center, the current density could be as low as 0.50 A/cm^2 , while the current density in the pore rim area could be as high as 3 A/cm^2 in the BP channel area. In the BP land area, the non-uniformity of current density is smaller, but the local current density variance is still significantly larger than the thicker PEM. For the $183\text{-}\mu\text{m}$ PEM, the current density variance is very limited. All the cases in Figs. 7 and 8 share the same overall current density of 2 A/cm^2 .

The high local current density might cause local water starvation in the PEM and intensive joule heat generation. As shown in Fig. 8a and b, a thinner PEM causes large water saturation variance. In the BP channel area, the water saturation could be as high as ~ 21 under the pore of anode electrode, but the water saturation sharply drops to ~ 15 under the solid part of the anode electrode. Furthermore, the local intensive joule heat caused by the non-uniform current density and water saturation will increase the local temperature inside PEMs, which may accelerate the degradation of ionomer. Additionally, the non-uniform water saturation may cause additional internal stress in PEMs because the PEM swells after water absorption. The internal stress potentially damages the local structure of PEMs and causes mechanical degradation.

We employed a validated model to predict the impacts of membrane thickness on the current and water profile in the membrane. It should be noted that the current and water profile highly depends on the pattern of the electrodes and local pore blockage. If we use a TTLGDL with a much smaller pore diameter and land width without any pore blockage, the profile of current and water is expected to be more uniform. Hence, the electrode pattern should be carefully designed if an ultrathin membrane is employed in PEMECs.

Overall, this study numerically investigated the negative impacts of BP lands and electrode lands, which has been partially observed in various experiments. On one hand, a relatively wide land of BP will cause a performance drop [30], local gas blockage [9], ohmic resistance increase [3], and gas saturation increase in PTLs [31]. On the other hand, Yu et al. precisely controlled the width of electrode lands and demonstrated that a wide electrode land will cause dramatically increased ohmic resistance of PEMECs [12]. These reported experimental results align well with the simulated results in this study, that is, both of BP lands and electrode lands are related with the blocked water/mass transport and locally dehydrated membrane.

5. Conclusion

In this study, we developed a 3D multiphysics model, and thoroughly validated it using experimental data to analyze and predict the non-homogeneous behaviors in PEMECs. We discovered that the design of electrodes has a significant impact on the distribution of water and current density within the PEM. The lands of the BP tend to partially block the pores of the 2D-structured TTLGDL, leading to a drastic reduction in local water saturation and current density. Furthermore, the electrode pattern also contributes to a non-uniform distribution of water and current density in the PEM. Specifically, the region beneath the land of the electrode exhibits a higher current density but lower water saturation, whereas the area beneath the electrode pores shows the opposite trend. Increasing the cell voltage exacerbates these non-uniform behaviors. Addressing local pore blockages can significantly enhance non-homogeneous behaviors by improving water and gas transport. Surprisingly, the thickness of the PEM also plays a crucial role in the distribution of water and current density. A thinner PEM tends to cause local water starvation and current crowding, potentially resulting in local hotspots and accelerated degradation.

It is crucial to note that these non-homogeneous behaviors can significantly impact performance and potentially accelerate the degradation of PEMECs. Therefore, more efforts are needed in both experimental and simulation-based approaches to further understand and mitigate these challenges effectively.

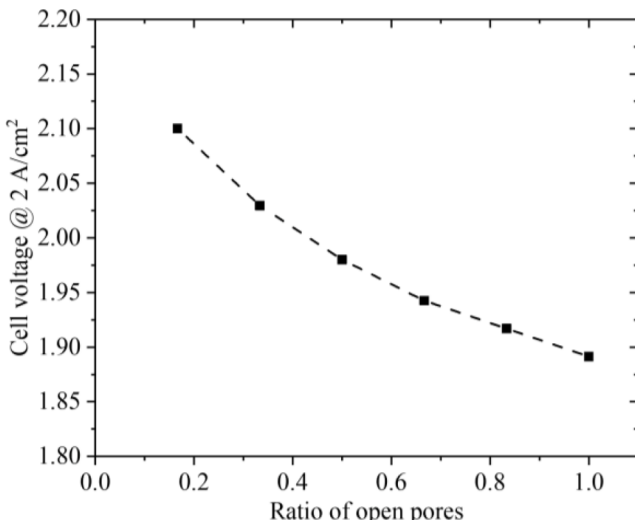


Fig. 6. Cell voltages with different ratios of open pores.

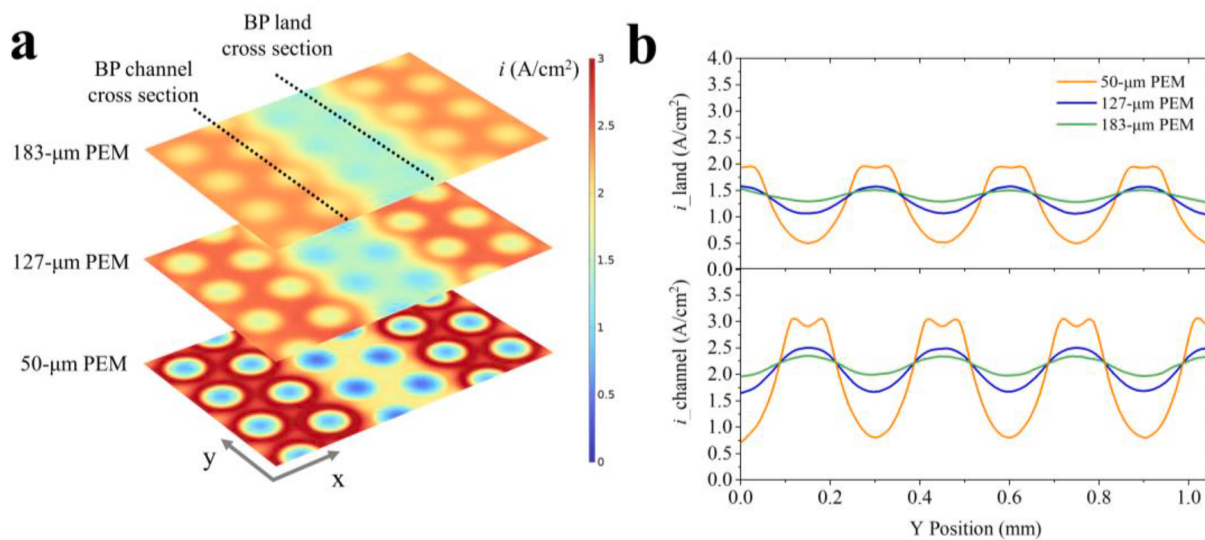


Fig. 7. a) current density profile of PEMs with different thicknesses; b) average current density in selected x-cross sections (BP land and channel as marked in Fig. 7a).

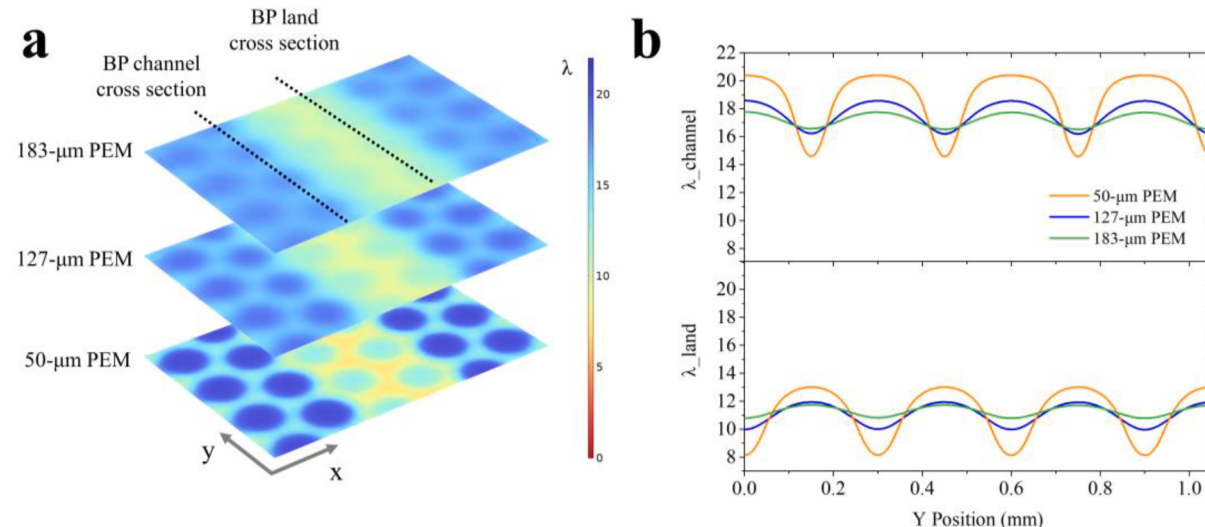


Fig. 8. a) water saturation profile of the PEM with different thicknesses; b) average water saturation in selected x-cross sections (BP land and channel as marked in Fig. 8a).

This manuscript presents the first 3D model with defined electrode pattern to describe the nonhomogeneous parameter distribution inside the membrane of PEMECs. However, as a device-level model some micro/nano scale morphology or phenomena (catalyst roughness/thickness, PTL/BP roughness, local gas nucleation, membrane deformation etc) are not considered. In the future, investigating how to link these micro/nano scale morphology or phenomena with a device-level model under a reasonable calculation efficiency is highly desired. Various challenges may be involved in this process, including unknown mechanisms, unmeasurable parameters, unaffordable calculation efficiency, etc.

CRediT authorship contribution statement

Weitian Wang: Writing – review & editing, Writing – original draft, Validation, Software, Methodology, Investigation, Formal analysis, Data curation, Conceptualization. **Jun Li:** Writing – review & editing. **Lei Ding:** Writing – review & editing. **Jiajie Wu:** Writing – review & editing, Software. **Hang Ma:** Writing – review & editing, Software. **Tony Shi:**

Writing – review & editing, Software, Methodology, Investigation. **Matthew Mench:** Supervision, Resources. **Feng-Yuan Zhang:** Writing – review & editing, Supervision, Resources, Project administration, Methodology, Funding acquisition.

Declaration of competing interest

The authors declare that they have no known competing financial interests or personal relationships that could have appeared to influence the work reported in this paper.

Acknowledgments

The authors greatly appreciate the support from U.S. Department of Energy's Office of Energy Efficiency and Renewable Energy (EERE) under the Hydrogen and Fuel Cell Technologies Office (HFTO) Award Number DE-EE0008426, DE-EE0008423 and DE-EE0009236. The authors also wish to express their appreciation to the Institute for Energy and Environment (IEE), Institute for a Secure and Sustainable

Environment (ISSE) and Center for Materials Processing at UTK.

Appendix A. Supplementary material

Supplementary data to this article can be found online at <https://doi.org/10.1016/j.enconman.2024.119222>.

Data availability

Data will be made available on request.

References

- [1] Vives AMV, Wang R, Roy S, Smallbone A. Techno-economic analysis of large-scale green hydrogen production and storage. *Appl Energ* 2023;346:121333.
- [2] Ueckerdt F, Verpoort PC, Anantharaman R, Bauer C, Beck F, Longden T, et al. On the cost competitiveness of blue and green hydrogen. *Joule* 2024;8:104–28.
- [3] Wang W, Ding L, Xie Z, Yu S, Capuano CB, Keane A, et al. 3D structured liquid/gas diffusion layers with flow enhanced microchannels for proton exchange membrane electrolyzers. *Energ Convers Manage* 2023;296:117665.
- [4] Wang W, Yu S, Li K, Ding L, Xie Z, Li Y, et al. Insights into the rapid two-phase transport dynamics in different structured porous transport layers of water electrolyzers through high-speed visualization. *J Power Sources* 2021;516:230641.
- [5] Yuan X-Z, Shaigan N, Song C, Aujla M, Neburchilov V, Kwan JTH, et al. The porous transport layer in proton exchange membrane water electrolysis: perspectives on a complex component. *Sustain Energy Fuel* 2022;6:1824–53.
- [6] Kang Z, Mo J, Yang G, Retterer ST, Cullen DA, Toops TJ, et al. Investigation of thin/well-tunable liquid/gas diffusion layers exhibiting superior multifunctional performance in low-temperature electrolytic water splitting. *Energ Environ Sci* 2017;10:166–75.
- [7] Zlobinski M, Schuler T, Büchi FN, Schmidt TJ, Boillat P. Transient and steady state two-phase flow in anodic porous transport layer of proton exchange membrane water electrolyzer. *J Electrochem Soc* 2020;167:084509.
- [8] Mo J, Kang Z, Retterer ST, Cullen DA, Toops TJ, Green Jr JB, et al. Discovery of true electrochemical reactions for ultrahigh catalyst mass activity in water splitting. *Sci Adv* 2016;2.
- [9] Wang W, Ding L, Xie Z, Yu S, Canfield B, Bender G, et al. Discovering reactant supply pathways at electrode/PEM reaction interfaces via a tailored interface-visible characterization cell. *Small* 2023.
- [10] Wrubel JA, Kang Z, Witteman L, Zhang F-Y, Ma Z, Bender G. Mathematical modeling of novel porous transport layer architectures for proton exchange membrane electrolysis cells. *Int J Hydrogen Energ* 2021;46:25341–54.
- [11] Han B, Mo JK, Kang ZY, Yang GQ, Barnhill W, Zhang FY. Modeling of two-phase transport in proton exchange membrane electrolyzer cells for hydrogen energy. *Int J Hydrogen Energ* 2017;42:4478–89.
- [12] Yu S, Li K, Wang W, Xie Z, Ding L, Kang Z, et al. Tuning catalyst activation and utilization via controlled electrode patterning for low-loading and high-efficiency water electrolyzers, *Small*, n/a 2107745.
- [13] Lee JK, Anderson G, Tricker AW, Babbe F, Madan A, Cullen DA, et al. Ionomer-free and recyclable porous-transport electrode for high-performing proton-exchange-membrane water electrolysis. *Nat Commun* 2023;14:4592.
- [14] Wang W, Li K, Ding L, Yu S, Xie Z, Cullen DA, et al. Exploring the impacts of conditioning on proton exchange membrane electrolyzers by *in situ* visualization and electrochemistry characterization. *ACS Appl Mater Interfaces* 2022.
- [15] Seweryn J, Biesdorf J, Schmidt TJ, Boillat P. Communication—neutron radiography of the water/gas distribution in the porous layers of an operating electrolyser. *J Electrochem Soc* 2016;163:F3009.
- [16] Falcão D, Pinto A. A review on PEM electrolyzer modelling: Guidelines for beginners. *J Clean Prod* 2020;261:121184.
- [17] Kang Z, Mo J, Yang G, Li Y, Talley DA, Han B, et al. Performance modeling and current mapping of proton exchange membrane electrolyzer cells with novel thin/tunable liquid/gas diffusion layers. *Electrochim Acta* 2017;255:405–16.
- [18] Han B, Mo J, Kang Z, Zhang F-Y. Effects of membrane electrode assembly properties on two-phase transport and performance in proton exchange membrane electrolyzer cells. *Electrochim Acta* 2016;188:317–26.
- [19] O'Hayre R, Cha S-W, Colella W, Prinz FB. *Fuel cell fundamentals*, John Wiley & Sons, 2016.
- [20] Lu Y, Wang W, Xie F. Investigation of oxygen evolution reaction kinetic process and kinetic parameters on iridium electrode by electrochemistry impedance spectroscopy analysis. *J Electroanal Chem* 2020;871:114281.
- [21] Dickinson EJ, Smith G. Modelling the proton-conductive membrane in practical polymer electrolyte membrane fuel cell (PEMFC) simulation: a review. *Membranes* 2020;10:310.
- [22] Motupally S, Becker AJ, Weidner JW. Diffusion of water in Nafion 115 membranes. *J Electrochem Soc* 2000;147:3171.
- [23] Luo Z, Chang Z, Zhang Y, Liu Z, Li J. Electro-osmotic drag coefficient and proton conductivity in Nafion® membrane for PEMFC. *Int J Hydrogen Energ* 2010;35: 3120–4.
- [24] Kusoglu A, Weber AZ. New insights into perfluorinated sulfonic-acid ionomers. *Chem Rev* 2017;117:987–1104.
- [25] Kientitz B, Yamada H, Nonoyama N, Weber AZ. Interfacial water transport effects in proton-exchange membranes, (2011).
- [26] Monroe CW, Romero T, Mérida W, Eikerling M. A vaporization-exchange model for water sorption and flux in Nafion. *J Membr Sci* 2008;324:1–6.
- [27] Ge S, Li X, Yi B, Hsing I-M. Absorption, desorption, and transport of water in polymer electrolyte membranes for fuel cells. *J Electrochem Soc* 2005;152:A1149.
- [28] Mo J, Kang Z, Yang G, Retterer ST, Cullen DA, Toops TJ, et al. Thin liquid/gas diffusion layers for high-efficiency hydrogen production from water splitting. *Appl Energ* 2016;177:817–22.
- [29] Chen Q, Wang Y, Yang F, Xu H. Two-dimensional multi-physics modeling of porous transport layer in polymer electrolyte membrane electrolyzer for water splitting. *Int J Hydrogen Energ* 2020;45:32984–94.
- [30] Zhang X, Higier A, Zhang X, Liu H. Experimental studies of effect of land width in PEM fuel cells with serpentine flow field and carbon cloth. *Energies* 2019;12:471.
- [31] Lee C, Lee J, Zhao B, Fahy K, LaManna J, Baltic E, et al. Temperature-dependent gas accumulation in polymer electrolyte membrane electrolyzer porous transport layers. *J Power Sources* 2020;446:227312.